

# The First Stray Light Corrected EUV Images of Solar Coronal Holes

Paul Shearer,\* Richard A. Frazin,† Alfred O. Hero III, and Anna C. Gilbert

*University of Michigan, Ann Arbor*

(Dated: June 3, 2019)

Coronal holes are the source regions of the fast solar wind, which fills most of the solar system volume near the cycle minimum. Removing stray light from extreme ultraviolet (EUV) images of the Sun's corona is of high astrophysical importance, as it is required to make meaningful determinations of temperatures and densities of coronal holes. Coronal holes tend to be dominated by the component of the stray light due to the long-range scatter caused by microroughness of telescope mirror surfaces, and this component has proven very difficult to measure in pre-flight characterization. In-flight characterization heretofore has proven elusive due to the fact that the detected image is simultaneously nonlinear in two unknown functions: the stray light pattern and the true image which would be seen by an ideal telescope. Using a constrained blind deconvolution technique that takes advantage of known zeros in the true image provided by a fortuitous lunar transit, we have removed the stray light from solar images seen by the EUVI instrument on STEREO-B in all four filter bands (171, 195, 284, and 304 Å). Uncertainty measures of the stray light corrected images, which include the systematic error due to misestimation of the scatter, are provided. It is shown that in EUVI, stray light contributes up to 70% of the emission in coronal holes seen on the solar disk, which has dramatic consequences for diagnostics of temperature and density and therefore estimates of key plasma parameters such as  $\beta$  and ion-electron collision rates.

One of the longest standing puzzles in astrophysics concerns the processes that energize the solar wind. The fast solar wind, which has a speed of  $\sim 800$  km/s near the Earth, emanates from EUV and X-ray faint regions in the Sun's atmosphere called *coronal holes* [1]. Physics-based modeling efforts to identify the processes that heat and accelerate the solar wind have met with very limited success [2]. It is likely that much more observational input will be required to adequately constrain the numerical models used to investigate this question. NASA's EUV imaging instruments (SOHO/EIT, TRACE, STEREO/EUVI, and SDO/AIA) provide a comprehensive data set covering 1 1/2 solar cycles that can provide powerful constraints on temperatures and densities in coronal holes [3]. However, coronal holes and other faint structures are severely contaminated with stray light, which must be corrected before these vast data sets may be utilized for this purpose.

All EUV imaging instruments are afflicted to some degree by long-range scattering, which distributes a haze of *stray light* over the whole imaging plane. This haze is not noticeable in the brighter areas of the image, but can completely overwhelm the emissions of faint regions. Stray light in EUV instruments generally arises from two sources: non-specular reflection from microrough mirror surfaces, and diffraction due to the pupil and a mesh obstructing the pupil [4]. This report describes a method for, and results of, correction of stray light in STEREO-B/EUVI, henceforth abbreviated as EUVI-B.

Stray light correction requires determination of the instrument's point spread function (PSF). The four EUVI channels (171, 195, 284, and 304 Å) have different opti-

cal paths and therefore different PSFs. Except for pixel-scale variations due to optical aberration (whereas the scattering of interest here is significant over ranges of hundreds of pixels), the EUVI PSFs are spatially invariant [4]. Thus, stray light contamination is modeled by convolution with the PSF, and the correction process is *deconvolution* [5].

The instrument PSFs are difficult to characterize experimentally due to the lack of a sufficiently strong EUV source, so they must be determined primarily from in-flight observations. While solar flare images (essentially very bright point sources) can provide significant information about the entrance aperture diffraction [6], they provide little information about the long range effects of scattering from microrough mirror surfaces. The best source of information about the nature of the long-range scatter is transiting bodies that do not emit in the EUV, so any apparent emission is instrumental in origin. DeForest et al. [7] used a Venus transit to estimate the mirror scattering in the TRACE instrument by fitting a truncated Lorentzian. Here, we present the first self-consistent determination of the mirror scattering via blind deconvolution, in which both the true solar image and various PSF parameters are taken to be unknown simultaneously. The source of information making this effort successful is Feb. 25, 2007 transit of the Moon across the Sun, as seen by STEREO-B, each exposure of which provided about 50,000 lunar disk pixels illuminated only by instrumental effects.

We characterize the scattering from the pupil, the pupil mesh, and the mirror microroughness with three separate PSFs:  $h^p$ ,  $h^g$ , and  $h_\varphi^m$  respectively, where  $\varphi$  denotes a set of parameters to be determined. Our model PSF  $h_\varphi$  is the convolution of these three PSFs:

$$h_\varphi = h^g * h^p * h_\varphi^m, \quad (1)$$

\* shearerp@umich.edu

† rfrazin@umich.edu

where

$$(u * v)(x) = \sum_{x' \in I} u(x - x')v(x') \quad (2)$$

denotes the convolution of two discrete functions  $u$  and  $v$  over the domain  $I \subset \mathbb{Z}^2$  indexing the  $2048 \times 2048$  array of CCD pixels. (We set  $u(x - x') = 0$  at pixels  $x - x' \notin I$ .) This model assumes that each scattering element is independent, neglecting phase correlations that arise as light propagates from the entrance aperture to the primary mirror. The PSFs  $h^p$  and  $h^g$  for the pupil and mesh were calculated using Fraunhofer diffraction theory, which states that the PSF for diffraction by an amplitude screen is (up to a proportionality constant) the squared modulus of the Fourier transform of the screen's transmittance function [8]. To determine the proportionality constants, each PSF is normalized to preserve flux, so that each PSF  $h$  obeys  $\sum_{x \in I} h(x) = 1$ .

We designed the model for the microrough scatter PSF  $h_\varphi^m$  to produce PSFs consistent with typical EUV scatter modeling and observations. In a typical EUV scatter model, a fraction  $\alpha$  of the light is not scattered ( $h_\varphi^m(0) = \alpha$ ), while the remaining  $1 - \alpha$  is scattered by broad, shallow wings [9]. The PSF wings are determined by the mirror surface height function's power spectral density, which is typically found to be roughly piecewise power-law (i.e., piecewise linear on a log-log plot; cf. [10], Fig. 10).

To construct a PSF consistent with these conditions, we choose a series of breakpoints  $1 = r_0 < r_1 < r_2 < \dots < r_b < \infty$ . The number of breakpoints,  $b = 8$ , was selected according to a  $\chi^2$  goodness of fit criterion. On each subinterval  $[r_{i-1}, r_i)$  the PSF's radial profile  $p_{\alpha, \beta}(r)$  is given by a power law:  $p_{\alpha, \beta}(r) \propto r^{-\beta_i}$ , where  $\beta_i \geq 0$ , and  $\beta = (\beta_1, \dots, \beta_b)$ . Fig. 1 gives the profile fit for the 171 Å PSF. A plausible fit could not be obtained with a radially symmetric PSF, so we generalized the model to include PSFs with elliptical cross sections. Let  $M_{s, \theta} \in \mathbb{R}^{2 \times 2}$  denote the matrix that dilates the plane by a factor of  $s$  along a line rotated  $\theta$  radians counterclockwise from the horizontal axis; then

$$h_\varphi^m(x) = p_{\alpha, \beta}(\|M_{s, \theta} \cdot x\|_2 + \delta), \quad (3)$$

where the constant  $\delta = 1$  was added to avoid the power law's singularity at the origin. The free parameters of the PSF model  $h_\varphi$  are then  $\varphi = (\beta, \alpha, \theta, s) \in \mathbb{R}^p$ , where  $p = b + 3 = 11$ .

To determine the PSF that best explains the lunar transit data, we described the observation process by a statistical image formation model and sought a maximum likelihood estimate of the PSF under this model. We let  $u^{\text{true}}$  denote the ideal image; that is,  $u^{\text{true}}(x)$  is the expected solar photon count that would be measured at pixel  $x$  by an ideal instrument. Due to scatter and the Poisson photon arrival process, the actual number of photon arrivals is a Poisson random variable with expected

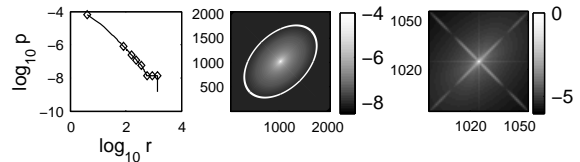


FIG. 1. An overview of the 171 Å PSF structure. All distances are in pixels. *Left*: the power-law profile function  $p_{\alpha, \beta}(r)$ , breakpoints marked. *Center, right*: the global PSF and the PSF core plotted with a  $\log_{10}$  color scale. An elliptical level set of the PSF is highlighted (*center*).

value  $h^{\text{true}} * u^{\text{true}}$ . The difference between the expected and the actual photon count is the photon noise  $n_{\text{phot}}$ . The observed photon count  $f$  deviates  $h^{\text{true}} * u^{\text{true}} + n_{\text{phot}}$  due to CCD dark current and read noise  $n_{\text{ccd}}$ . Based on histograms of dark images, we find  $n_{\text{ccd}}$  is reasonably modeled as a Gaussian white noise process with constant variance  $\sigma_{\text{ccd}}^2 \approx 1$  digital number (DN). The variance must be divided by the photometric gain factor (the recorded DN per incident photon) to obtain the CCD noise level in units of photons. Combining  $n_{\text{phot}}$  and  $n_{\text{ccd}}$  into a single variable  $n$ , we obtain the statistical image formation model

$$f = h^{\text{true}} * u^{\text{true}} + n. \quad (4)$$

We would like to find a maximum likelihood estimate of the PSF under the model (4), but the Poisson-Gaussian distribution of  $n$  leads to a difficult large-scale nonlinear optimization problem. We therefore apply a variance stabilizing transform (VST) to make  $n$  approximately standard normal (mean zero and variance one), which leads to an easier least-squares problem. A VST for a Poisson-Gaussian random variable where the Gaussian has variance  $\sigma^2$  is derived in [11]:  $\text{vst}(I) = 2\sqrt{I + \frac{3}{8} + \sigma^2}$ . If the VST is applied to both sides of (4) with  $\sigma^2 = \sigma_{\text{ccd}}^2$ , we obtain

$$\text{vst}(f) \approx \text{vst}(h^{\text{true}} * u^{\text{true}}) + n_{\text{vst}}, \quad (5)$$

where, for each  $x$ ,  $n_{\text{vst}}(x)$  is roughly standard normal [11]. The approximation begins to break down when  $I \lesssim 5$  photons [11], but this only occurs far from the solar disk in the lunar transit images. In these low-intensity regions we replace the observed image pixel value with a local average of sufficient size that the total photon counts exceed 5 in the averaged neighborhood.

We found an estimate  $h_\varphi$  of the EUVI-B PSF  $h^{\text{true}}$  by solving a maximum likelihood blind deconvolution problem on a series of 8 images  $f_1, \dots, f_8$  from the lunar transit series. We assume the scatter-free images  $u_i^{\text{true}}$  are positive everywhere and zero on the lunar disk pixels  $Z_i$ , leading to the constraints

$$u_i^{\text{true}} \geq 0, \quad u_i^{\text{true}}(Z_i) = 0, \quad i = 1, \dots, 8. \quad (6)$$

The lunar disk was identified by detecting its edge pixels with gradient thresholding, then fitting a circle to the detected edge pixels. An approximate maximum likelihood

estimate for the PSF  $h_\varphi$  and images  $\{u_i\}$  is obtained by solving

$$\begin{aligned} & \underset{\varphi=(\beta,\alpha,s,\theta), \{u_i\}}{\text{minimize}} && \sum_{i=1}^8 \| \text{vst}(h_\varphi * u_i) - \text{vst}(f_i) \|^2 \\ & \text{subject to} && u_i \geq 0, u_i(Z_i) = 0 \text{ for all } i, \\ & && \beta \geq 0, 0 \leq \alpha \leq 1. \end{aligned} \quad (7)$$

Since each  $u_i$  is a  $2048 \times 2048$  image, this problem has over 32 million variables and is intractable by general-purpose numerical methods. However, if the vst is removed, the objective is quadratic in  $u$  for fixed  $\varphi$ . The variable projection method is efficient on problems of this type [12], but does not handle bounds on  $u$ . We solved this problem with a novel variant that handles the addition of vst and the bounds on  $u$  approximately.

Fig. 1 shows a log-log plot of the  $171 \text{ \AA}$  profile function obtained by blind deconvolution, along with views of the global PSF and its core. Note that the profile is constant for  $200 < r < 1200$  pixels, implying significantly more long range scatter than a constant power law exponent would predict. The global PSF is dominated by the elliptical power law decay, although a contribution from the pupil and mesh PSFs is visible near the PSF core.

Once we determined the PSF from blind deconvolution, we were able to correct any observed EUVI-B image  $f$  via more standard deconvolution methods. Let  $\mathcal{C}(h) : \mathbb{R}^I \rightarrow \mathbb{R}^I$  denote the linear operator that convolves an input image  $u$  with a fixed PSF  $h$ :  $\mathcal{C}(h)u = h * u$ . The stray light correction of a given image  $f$  is obtained by applying the inverse of  $\mathcal{C}(h)$  to  $f$ :

$$u = \mathcal{C}(h)^{-1}f. \quad (8)$$

The inverse operator does not exist for arbitrary  $h$ . However, our PSFs have an origin value  $h(0) > 1/2$ , which makes  $\mathcal{C}(h)$  diagonally dominant and invertible. The inversion of (8) can be performed with the conjugate gradient method in less than a minute on a laptop.

We measured the effectiveness of our stray light correction using cross-validation (CV). For each of the 8 images  $f_i$ , we determined a PSF  $h_i$  by solving (7) with  $f_i$  removed from the dataset. We then calculated the stray light corrected CV image  $u_i^* = \mathcal{C}(h_i)^{-1}f_i$ . Note that both  $h_i$  and  $u_i^*$  are calculated without any assumption of a zero lunar disk in image  $i$ , so the values of  $u_i^*$  on the lunar disk represent an independent check on the correction's effectiveness. In Fig. 2 we compare the lunar disks of  $f_i$  and  $u_i^*$  in  $171 \text{ \AA}$ . We find that the lunar disk values after deconvolution are very strongly clustered near zero, as seen in a histogram of the lunar disk values (*center right*).

To estimate the error in the corrected images, we decompose the total error  $\varepsilon = u - u^{\text{true}}$  into components due to noise and PSF error, and estimate their contributions separately. To obtain the decomposition we substitute (4) into (8) and introduce the PSF error variable  $\delta h = h - h^{\text{true}}$ , obtaining

$$\varepsilon = u - u^{\text{true}} = \mathcal{C}(h)^{-1}\mathcal{C}(\delta h)u^{\text{true}} + \mathcal{C}(h)^{-1}n. \quad (9)$$

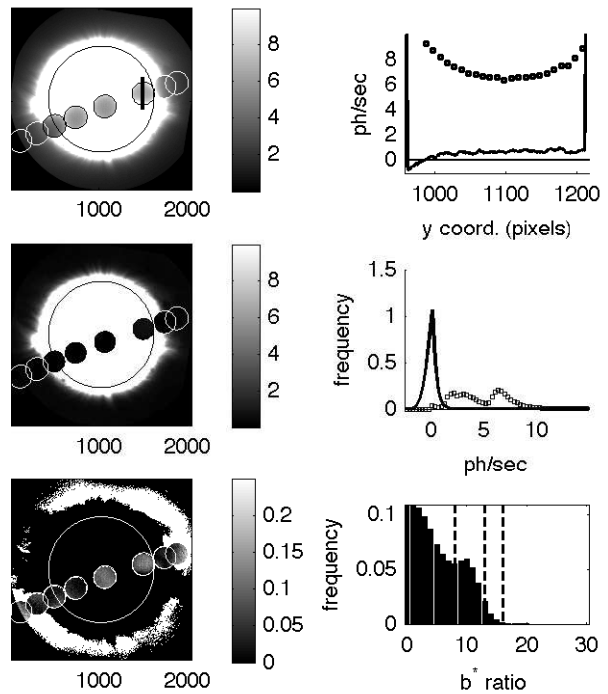


FIG. 2. The lunar transit before and after stray light correction ( $171 \text{ \AA}$ ). The lunar and solar limbs are outlined for reference. *Top left*: The lunar disks from the eight transit images  $f_i$  superimposed on the first image of the series,  $f_1$ . The colorbar is in photons per second (ph/sec) and has a low upper limit to show the stray light on the lunar disks. The black line segment identifies a series of pixels whose intensity values are plotted to the right (see *top right*). *Center left*: The lunar disks from the CV images  $u_i^*$  superimposed on  $u_1$ . *Bottom left*: Map of the  $b_i^*$  values on the 8 lunar disks. Separate from the lunar disks, the pixels where  $u_1 < 0.25f_1$  are highlighted in white. *Bottom right*: Normalized histogram giving the distribution of the  $b_i^*$  values. The dashed vertical lines indicate the 68<sup>th</sup>, 95<sup>th</sup>, and 99.7<sup>th</sup> percentile values. *Center right*: Normalized histograms giving the distribution of lunar disk intensities before correction (solid) and after (squares). *Top right*: Intensity along the *top left* vertical black line segment before correction (squares) and after (solid).

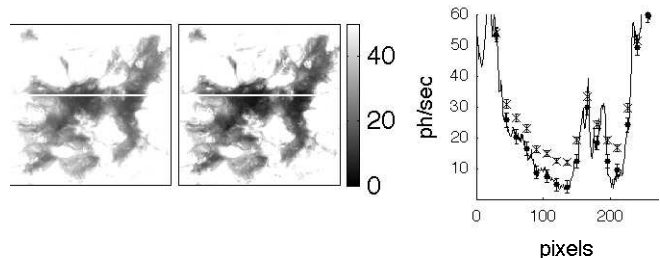


FIG. 3. Stray light correction of an on-disk coronal hole observed by EUVI-B on Nov. 21, 2008. *Left and center*: The observed data  $f$  and corrected data  $u$  (ph/sec). *Right*: Line plots of  $f$  (crosses) and  $u$  (solid line) along the white line segment. The horizontal axis is in pixels relative to the segment's left endpoint. Error bars are given every 20 pixels.

The right hand side's first term gives the error due to PSF misestimation, which we name  $\varepsilon_{\text{psf}}$ . The second,  $\varepsilon_{\text{noise}}$ , is the noise in the corrected image.

To estimate  $\varepsilon_{\text{psf}}$ , we first applied an  $8 \times 8$  moving average filter to  $u$  and  $f$  to reduce noise, leaving the  $\varepsilon_{\text{psf}}$  term dominant. (Averaging also reduces  $\varepsilon_{\text{psf}}$  on small scales, potentially leading to underestimation of the error. However, we are only interested in the large-scale effect of stray light, and on large scales,  $\varepsilon_{\text{psf}}$  is unaffected by averaging.) Next, we sought an estimate  $\sigma_{\text{psf}}$  of  $\varepsilon_{\text{psf}}$  proportional to the magnitude of the stray light correction  $|u - f|$ :

$$|u - u^{\text{true}}| \leq B|u - f| = \sigma_{\text{psf}}. \quad (10)$$

We use the bounding term  $B|u - f|$  because it shares two distinctive properties with  $\varepsilon_{\text{psf}}$ : both are approximately invariant if  $u^{\text{true}}$  is changed by scaling or addition of a constant. These invariance properties help ensure that an empirical bound based on lunar transit images alone will continue to be valid for other solar images.

We determined the constant  $B$  by requiring that (10) hold true over almost all of the lunar disk pixels of  $f_i$  and  $u_i^*$ . Setting  $u = u_i^*$ ,  $f = f_i$ , dividing both sides by  $|u_i^* - f_i|$ , and noting that  $u_i^{\text{true}} = 0$  on the lunar disk, we find  $|u_i^*|/|u_i^* - f_i| \leq B$  is required on the lunar disk pixels. We call the left-hand side ratio  $b_i^*$ , and collect the values of  $b_i^*$  on the 8 lunar disks into a histogram. A normalized histogram for 171 Å is given in Fig. 2, *middle right*, and values at the 68<sup>th</sup>, 95<sup>th</sup>, and 99.7<sup>th</sup> percentiles, corresponding to the first three standard deviations of a Gaussian, are 0.08, 0.13, and 0.16. We set  $B$  equal to the 95<sup>th</sup> percentile of the histogram, which gives a conservative  $2\sigma$  error bound robust to outliers. To estimate the contribution of noise to the error, we analytically calculate its covariance matrix using the known variance of  $n$ . The diagonal of this covariance matrix,  $\sigma_{\text{noise}}^2$ , is our estimate of the squared error due to noise. We add the two independent errors in quadrature to obtain the final error estimate  $\sigma$ :  $\sigma^2 = \sigma_{\text{psf}}^2 + \sigma_{\text{noise}}^2$ .

In Fig. 3 we examine a coronal hole before and after stray light correction. The stray light corrected coronal hole is significantly dimmer: the percent change  $(u - f)/f$

ranges from  $-40$  to  $-70\%$  over most of the coronal hole, implying that 40-70% of the apparent coronal hole emissions are stray light. The plot of intensity versus position (*right*) contains the error bars  $\sigma$ . Note that they are small relative to the size of the correction, which is representative of typical results.

We have obtained PSFs for all 4 bands of STEREO-B/EUVI using lunar transit data, which enables us to correct all EUVI-B images for stray light and provide uncertainties. Similar methods may be applied to treat the stray light problems in the other solar EUV imaging instruments (SOHO/EIT, TRACE, STEREO-A/EUVI, SDO/AIA), and this work will be reported in more detail in discipline specific journals. The plasma diagnostics available from EUV images are related to the electron temperature  $T_e$  and density  $n_e$  because (assuming electron impact excitation) the intensity of the emission in images from the  $k^{\text{th}}$  spectral band is  $I_k \propto \int_{\text{LOS}} dl n_e^2(l) Q_k(T_e(l))$ , where  $Q_k(T_e)$  comes from an optically thin plasma emission model and  $\int_{\text{LOS}} dl$  represents integration along the line-of-sight [13]. This relationship may be utilized to create 3D tomographic maps of  $n_e$  and  $T_e$  [3]. A downward correction of the observed intensity causes a proportional reduction of the estimated value of  $n_e$ , indeed, analysis of the 171, 195 and 284 Å intensities show a downward revision of the coronal hole column density  $[\int_{\text{LOS}} dl n_e^2(l)]^{1/2}$  of  $\sim 40\%$ . The effect on the estimated  $T_e$  is more complex.

An especially significant consequence of stray light correction is the removal of the haze seen above the limb (Fig. 2, *upper left*), which is not present in the corrected images (*center left*). Stray light correction removed 75% or more of the apparent emission in much of the off-limb part of the image, as indicated by the white pixels in Fig. 2 (bottom left). Thus, the stray light correction causes a dramatic steepening of the profile function  $n_e(h)$  (where  $h$  is the height above the photosphere). The specific impact of stray light correction, including constraints on solar wind models from the corrected profiles  $n_e(h)$ ,  $T_e(h)$ , is currently under investigation. Obvious consequences include reduction of the plasma  $\beta$ , electron-ion collision rates, and the mass of solar wind plasma requiring acceleration.

- 
- [1] A. S. Krieger, A. F. Timothy, and E. C. Roelof, *Solar Physics* **29**, 505 (1973).
- [2] S. Cranmer, *Space Sci. Rev.* (2010).
- [3] R. A. Frazin, A. M. Vásquez, and F. Kamalabadi, *The Astrophysical Journal* **701**, 547 (2009).
- [4] R. A. Howard *et al.*, *Space Sci. Rev.* **136**, 67 (2008).
- [5] J. L. Starck, E. Pantin, and F. Murtagh, *PASP* **114**, 1051 (2002).
- [6] S. Gburek, J. Sylwester, and P. Martens, *Solar Physics* **239**, 531 (2006).
- [7] C. E. DeForest, P. C. H. Martens, and M. J. Wills-Davey, *The Astrophysical Journal* **690**, 1264 (2009).
- [8] J. W. Goodman, *Introduction to Fourier Optics*, 2nd ed. (McGraw-Hill, 1996).
- [9] C. G. Krautschik, M. Ito, I. Nishiyama, and S. Okazaki, *Proc. SPIE* **4688**, 289 (2002).
- [10] D. Martínez-Galarce, J. Harvey, *et al.*, *Proc. SPIE* **7732**, 773237 (2010).
- [11] F. Murtagh, J.-L. Starck, and A. Bijaoui, *Astronomy and Astrophysics* **112**, 179 (1995).
- [12] G. Golub and V. Pereyra, in *Institute of Physics, Inverse Problems* (2002) pp. 1–26.
- [13] J. C. Brown, B. N. Dwivedi, *et al.*, *Astronomy and Astrophysics* **249**, 277 (1991).